Tectonophysics 554-557 (2012) 105–113

Contents lists available at SciVerse ScienceDirect

Tectonophysics

journal homepage: www.elsevier.com/locate/tecto

The seismically active Atalanti fault in Central Greece: A steeply dipping fault zone imaged from magnetotelluric data

Alexandros Savvaidis [a,*], Maxim Yu. Smirnov [b,1], Markos D. Tranos [c,2], Laust B. Pedersen [b,1], Gerasimos Chouliaras [d,3]

[a] Institute of Engineering Seismology and Earthquake Engineering, EPPO, P.O. Box 53, Finikas, 55102 Thessaloniki, Greece
[b] Uppsala University, Department of Earth Sciences, Geophysics, Villavagen 16, 75236 Uppsala, Sweden
[c] Department of Geology, School of Geology, Aristotle University of Thessaloniki, 54124 Thessaloniki, Greece
[d] Institute of Geodynamics, National Observatory of Athens, P.O. Box 20048 Thissio, 11810 Athens, Greece

ARTICLE INFO

Article history:
Received 13 March 2011
Received in revised form 9 April 2012
Accepted 2 June 2012
Available online 13 June 2012

Keywords:
Magnetotelluric method
Crustal structure
Atalanti fault
Extensional fault

ABSTRACT

The WNW–ESE striking Atalanti fault is one of the large fault segments of the ca. 110-km-long WNW–ESE trending Sperchios–Chalkis Fault System that subsided along the NE slopes of the Kalidromon and Chlomo Mts. in Central Greece forming an extensive graben similar to the Corinthiakos Gulf. Although, the fault is characterized by recent seismic activity, it has up to now not been investigated by means of geophysical methods that could define the geometrical features of the structure in depth.

Magnetotelluric measurements performed along three 14-km-long profiles A, B, and C and across the fault with a total of 28 stations indicate that its geoelectric strike is WNW–ESE. Two-dimensional bimodal and the determinant of the impedance tensor inversions were applied to the data. The best data fit was achieved using the determinant data. The resulting 2D models were further interpreted both separately and all together in order to define the geometry of the structure down to a depth of several kilometers.

The derived resistivity model defines that the Atalanti fault strikes WNW–ESE and forms a damage zone that contains two high-angle fault branches that dip at angles of 60° and 80° respectively. Thus, the interpreted geometry of the Atalanti fault and consequently the Sperchios–Chalkis Fault System differs from previous interpretation of a low-angle extensional crustal structure. In addition, the electrical resistivity model indicates the subsidence of the overthrust of the Internal Hellenides over the Parnassos zone toward the NNE from a depth of 2 km to deeper crustal levels due to the Atalanti fault.

1. Introduction

The Hellenic peninsula exhibiting high seismic activity is intensely stretched along the N–S to NNE–SSW trend above the Hellenic Subduction Zone through the activation of large zones of weakness that accommodate large amount of the contemporary crustal deformation (Fig. 1a), especially in the inner or along the Hellenic orogen as the latter is defined by its backbone, the Pindos Mountain Range (PMR), Fig. 1(a). This conclusion is supported by the fact that their activation has been associated with very big and disastrous historical and instrumental earthquakes (Papazachos et al., 2001). Among these fault zones, the most prevalent ones are exposed in Central Greece, where they transect obliquely the NNW–SSE orogenic fabric forming km-long segmented fault zones such as the Corinth Gulf Fault System (C FS), the Sperchios–Chalkis Fault System (S–C FS) and the Kremasta–Sperchios Fault System (K–S FS) (Fig. 1a, b).

During the last two decades, several fault zones have been intensely investigated in Greece, especially in cases when they were associated with strong earthquakes. These investigations were based mainly on the methods and approaches of neotectonics and seismology. An interesting issue arising from this research concerns the dip angle of the faults activated within these fault systems since the Late Tertiary. In particular, Kranis and Papanikolaou (2001) and Papanikolaou and Royden (2007) suggest that the NE-dipping Parnassos Fault Zone (or Boetikos–Kifissos detachment), that bounds the NE slopes of the Parnassos Mt., dips to the NE at angles of ~30°. According to the same authors, the Sperchios–Chalkis Fault System (or Ag. Konstantinos detachment) dips northeast at angles between 20° and 45°. Karastathis et al. (2007) studied the shallow part of the seismically active Atalanti fault, a fault segment of the Sperchios–Chalkis Fault System, and estimated dip angles of ~45°–49° for it. On the other hand, Sakellariou et al. (2007) suggested that the NW–SE striking faults that bound the Central Basin of North

* Corresponding author. Tel.: +30 2310476085.
E-mail addresses: alexandros@itsak.gr (A. Savvaidis), maxim.smirnov@oulu.fi (M.Y. Smirnov), tranos@geo.auth.gr (M.D. Tranos), laust.pedersen@geo.uu.se (L.B. Pedersen), g.choul@noa.gr (G. Chouliaras).
[1] Tel.: +46 18501110.
[2] Tel.: +30 2310998482.
[3] Tel.: +30 2103490180.

0040-1951/$ – see front matter © 2012 Elsevier B.V. All rights reserved.
doi:10.1016/j.tecto.2012.06.002

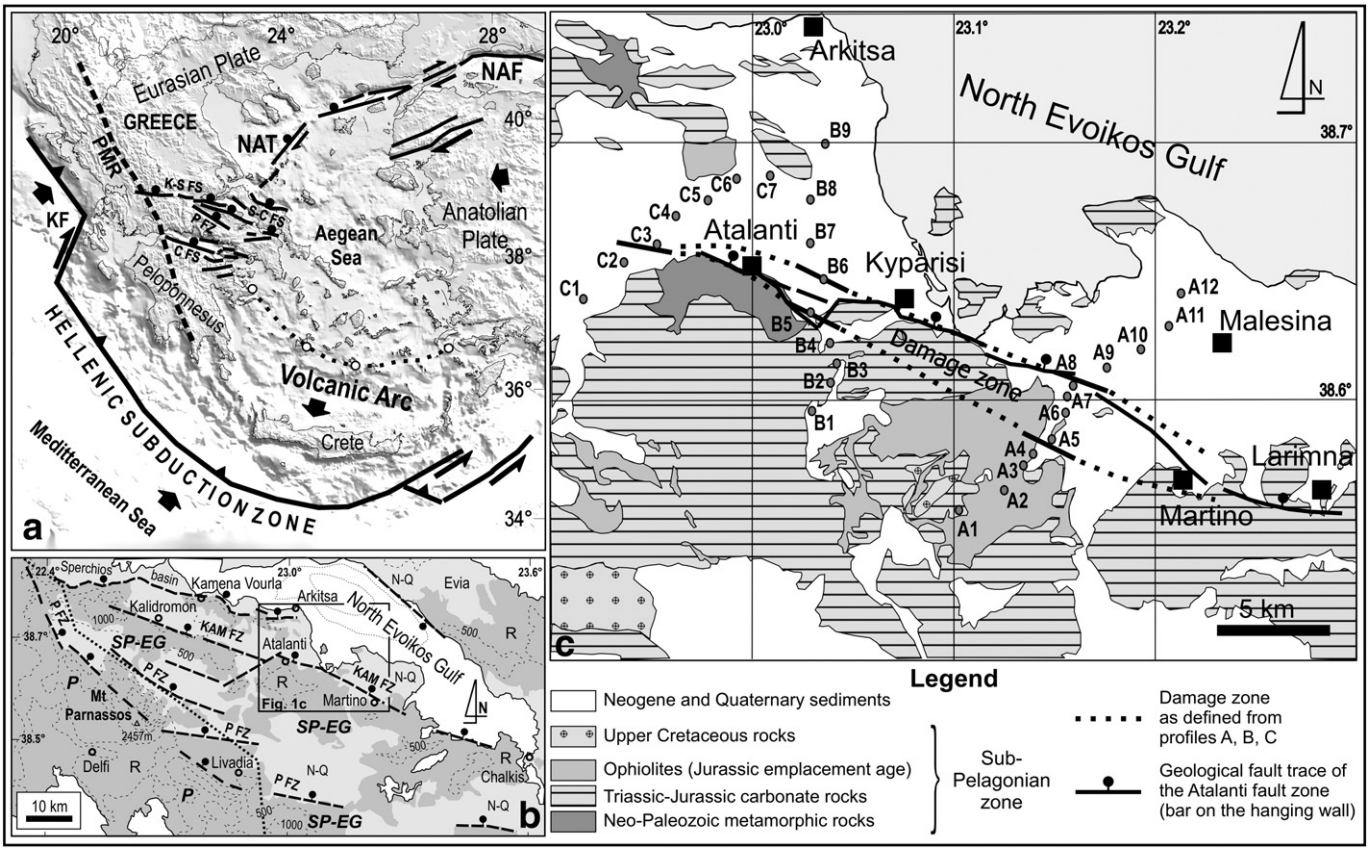

Fig. 1. (a) Digital relief of broader Aegean area showing the main geotectonic setting (C FS: Corinth Fault System; KF: Kefalonia transform Fault, K–S FS: Kremasta–Sperchios Fault System; NAF: North Anatolian Fault, NAT: North Aegean Trough; P-FZ: Parnassos Fault Zone, PMR: Pindos Mountain Range, S–C FS: Sperchios–Chalkis Fault System). (b) Simplified geological map showing the geotectonic zones and structures of the broader study area. Study area shown in 1c is marked with a frame, whereas dashed lines are height contour lines (KAM-FZ: Kalidromon–Atalanti–Martino Fault Zone; N–Q: Neogene–Quaternary sediments; P: Parnassos Zone; P-FZ: Parnassos Fault Zone; R: alpine rocks; SP-EG: Sub-Pelagonian or zone of Eastern Greece). (c) Geological map of the study area showing the Atalanti fault. The position of the MT sites is given with dots and labeled A1–12, B1–9 and C1–7 corresponding to profiles A, B, and C respectively.

Evoikos Gulf are high-angle ones. The extensional faults that crop out south of the Corinth Gulf, in northern Peloponnesus, dip at angles 45°–55° (Armijo et al., 1996) or 40°–50° Sorel (2000). Although, among the low-angle faults few have been documented as active ones (see Collettini, 2011 and reference therein), the association between the low-angle normal faults, ductile shear zones, and the exhumation of metamorphic rocks as metamorphic core complexes has revolutionized the concepts of lithospheric extension over the past decade (Axen et al., 1999 and references there in). As a result, based on the dip angle of the faults, different modes of faulting have been proposed for the large fault systems exposed in Central Greece. For example, Sorel (2000) suggested that the steeper faults of the Corinth Gulf Fault System branch into the northern Peloponnesus detachment that is still active under the gulf. In contrast, Armijo et al. (1996) proposed a mechanical model of the lithosphere in which the steep faults of the Corinth Gulf Fault System played the major role in the formation of the rift.

The seismically active fault zones in Central Greece are very crucial to define either the low-angle or high-angle geometry of the corresponding zones and consequently to better understand the Late Tertiary–Quaternary faulting that gave rise to the stretching of the Aegean plate.

It is noteworthy to mention that though the geophysical methods can contribute to the visualization of the large scale crustal structures at depth, they have hardly been used as an exploratory tool in Greece. Only recently, a geophysical study was undertaken along the Atalanti fault segment (Karastathis et al., 2007), but only the upper few hundred meters were imaged.

The magnetotelluric (MT) method has been applied recently in the study of large fault zones because it is sensitive to vertical/subvertical structures characterizing many fault systems. Furthermore, the fault zones are often associated with well conducting geoelectrical structures (Ritter et al., 2005) like the San Andreas Fault in the USA (Becken, 2010; Becken et al., 2008a, 2011; Bedrosian et al., 2002; Unsworth and Bedrosian, 2004; Unsworth et al., 1997), the Snowbird Tectonic Zone and the Tintina Fault in Canada (Jones et al., 2002; Ledo and Jones, 2002) and the Dead Sea Transform Fault in Jordan (Maercklin et al., 2005; Ritter et al., 2003; Weber et al., 2009). All these studies were successful in revealing new important information about the geometry of the fault zones.

Therefore, our objective is to image in depth the geometry of the seismically active Atalanti fault, a fault segment of the Sperchios–Chalkis Fault System, by using the magnetotelluric method and thus to understand the geometry of the large seismically active Sperchios–Chalkis Fault System.

Additionally, we try to interrelate the geometry of the MT model of this fault system in Central Greece with available seismological and neotectonic information in order to better understand the crustal processes that formed the transect in the orogenic fabric.

2. Geological and seismotectonic setting

The Greek mainland is a rapidly extending region with normal-faulting earthquakes as large as Mw = 6.5 corresponding to slip on approximately 10–30 km long faults (Mountrakis et al., 2006; Papazachos et al., 2001). However, these faults are parts of much larger fault zones or fault systems in Central Greece such as the 80-km-long Southern Thessaly Fault Zone (Mountrakis et al., 1993), the 100-km-long Kremasta–Sperchios Fault System (Kilias et al., 2008), the ca. 110-km-long Sperchios–Chalkis Fault System and the 120-km-long

Corinthiakos Fault System (Papanikolaou and Royden, 2007; Roberts, 1996; Roberts and Jackson, 1991). Another feature of these zones is that they interrupt the basin-and-range topography resulted by the Late Tertiary activation of the orogen-parallel NW–SE striking extensional faults.

More precisely, in Central Greece, between 38°N and 40°N, the large normal faults occur with a general WNW–ESE or E–W strike and approximately N–S trending slip vectors (Hatzfeld, 1999; Kilias et al., 2008; Mountrakis et al., 1993; Papazachos et al., 1998; Roberts and Jackson, 1991). The Sperchios–Chalkis graben is a major half-graben, submarine in larger parts, which has been formed by the activation of km-long fault segments of the homonymous fault system.

The region of Central Greece, as a part of the Hellenic orogen, is dominated by the Tertiary alpine nappe tectonics due to the collision between Apulia and Eurasia plates (Mountrakis, 2010). In particular, the broader study area is built up by the sheets of the Inner Hellenides (SubPelagonian or zone of Eastern Greece (SP-EG) and Pelagonian zones) over the external Hellenides (Parnassos zone, *P*) (Fig. 1b). More precisely, the Pelagonian zone represents a Cimmerian continental block consisting of Paleozoic or older crystalline rocks onto which Neo-Paleozoic metavolcanosedimentary rocks have been deposited. The latter, indicating continental rifting was followed by Triassic–Jurassic carbonate rocks. These rocks represent either a carbonate-platform sedimentation (in Pelagonian zone) or pelagic sedimentation (in SubPelagonian zone) toward the oceanic crust. In the Late Jurassic–Early Cretaceous times due to the Cimmerian orogeny, a large ophiolite sheet has been emplaced onto the continent indicating a destruction and obduction of the oceanic crust (Mountrakis, 1986). The ophiolites were unconformably overlaid by post-Cimmerian Cretaceous limestones and flysch rocks. All the above described rocks have eventually been evolved in the Tertiary alpine orogeny that formed the Hellenic orogen (Mountrakis et al., 2006). The Parnassos zone consists of Mesozoic carbonate-platform sequence succeeded by a Paleocene to Eocene flysch sediments. A characteristic feature of the zone is the three main bauxite horizons that have been recognized within the carbonate sequence with the most recent one that formed in the Late Cretaceous.

The NW–SE trending Parnassos Fault Zone (P FZ) consisting of NW–SE striking faults lower the NE slopes of the Parnassos Mt. forming small basins easterly of the Parnassos Mt. (Rondogianni-Tsiambaou, 1984). These faults, revealing stepping geometry, could be also considered as a part of the Sperchios–Chalkis Fault System, but seems to be related to the earlier stages of the fault system.

The WNW–ESE striking Kalidromon–Atalanti–Martino Fault Zone (KAM FZ) comprising the Kalidromon, Atalanti and Martino fault segments is the longest and most rectilinear fault line of the Chalkis–Sperchios Fault System (Fig. 1b). These, approximately 30-km-long fault segments, cut through the Neo-Paleozoic and Mesozoic rocks and mostly the extensive outcrops of the Mesozoic carbonates of the SubPelagonian zone. The escarpments formed in these rocks are more degraded in comparison to those of the Sperchios–Arkitsa Fault Zone (Goldsworthy and Jackson, 2001). Two earthquake events that occurred in 1894, on the 20th and the 27th of April have been related to the Atalanti fault segment (Ambraseys and Jackson, 1990; Papazachos and Papazachou, 2003; Skouphos, 1894). More than 250 people were killed and thousands of houses in the broader area collapsed (Mitsopoulos, 1895). Although no high seismicity was recorded after these events, there is a big interest in the scientific community to work in this area in order to understand the rupture conditions of this seismically active region.

Because of these disastrous earthquake events, the Kalidromon–Atalanti–Martino Fault Zone (KAM FZ) has attracted the interest of several researchers. Poulimenos and Doutsos (1996) suggest that the fault zone is characterized by significant bends at an angle of N125°E, from which new ruptures could be developed with a main strike of N115°E. However, they suggest that the main segments of the fault zone strike N130°E and subsidiary N75°E. Similar WNW–ESE strikes are given by Ganas et al. (1998) who used satellite images in their interpretation, and by Pantosti et al. (2001, 2004) who used aerial photographs, surface ruptures and paleoseismological criteria. Papazachos et al. (2001) using seismological information propose that the fault zone strikes N114°E and dips to NE at an angle of 50°, whereas Pavlides et al. (2004) give strikes for the Atalanti fault ranging from N109°E to N138°E and dip angles of 60–72° toward the NNE–NE.

The faults in the broader area are characterized by normal-type activations as indicated by several neotectonic studies (Ganas et al., 1998; Jackson and Mckenzie, 1999; Kilias et al., 2008; Kranis, 1999; Pavlides et al., 2004; Rondogianni-Tsiambaou, 1984) and seismological ones (Kemetzetzidou, 1996; Louvari, 2000; Papazachos et al., 2001). These activations have been driven by an extensional stress regime with the least principal stress axis (σ_3) oriented NNE–SSW to N–S.

The exposed rocks in the study area, following the main geological investigation (Maratos, 1965), belong to the SubPelagonian zone (or zone of Eastern Greece) and from bottom to top can be briefly described as follows (Fig. 1c):

(a) Neo-Paleozoic low-grade metamorphic basement that crops out in the mountainous area south of Atalanti village. It consists of Permo-Carboniferous metaclastic rocks, i.e., phyllites, quartzites, etc. that unconformably overlie Pre-Paleozoic to Paleozoic highly metamorphosed crystalline rocks such as gneisses, amphibolites and orthogneisses.
(b) Triassic–Jurassic carbonate rocks that are transgressively deposited onto the meta-clastic rocks,
(c) Ophiolite rocks that include mainly serpentinites, peridotites and dunites of Jurassic age of emplacement intermixed with deep-sea sediments,
(d) Upper Cretaceous rocks that were deposited transgressively onto (b) and (c) rocks. They include basal conglomerates and carbonates, the thickness of which does not exceed 300 m, which were overlain by Upper Cretaceous flysch-type sediments.
(e) Onto these alpine rocks that constitute the pre-Neogene basement in the area, Neogene, mostly Pliocene coal-bearing continental sediments and Quaternary sediments have been deposited.

3. Magnetotelluric data

Magnetotelluric soundings were acquired in 2002 along three profiles that cover the Atalanti fault along its full length (Fig. 1c). Profile A strikes NNE–SSW and crosses the central part of the fault zone, nearly perpendicular to the strike of the fault as defined from the seismological and geological data. Profile B striking almost N–S was positioned on that part of the fault zone, where a well established bend has been defined both from field (Poulimenos and Doutsos, 1996) and satellite data (Ganas et al., 1998). This location was selected in order to visualize in depth the possible geometrical deflections arising from this bending. The last profile C striking NE–SW is located close to the western tip of the Atalanti fault, i.e., toward the Kalidromon fault. That was done in order to understand better the 3D geometry of the Kalidromon–Atalanti fault. The strike of the profile has been chosen such as to be close to orthogonal to both NW–SE and WNW–ESE fault orientations in order to define better the 3D effect caused by them.

Three instruments were operating simultaneously in order to employ the remote reference technique. During the measurements at least one station was kept as far as possible from densely populated areas to reduce the influence of cultural noise. The station was later used as a remote reference site. The minimum distance between measurement sites and reference station was 5 km. All together data from 28 sites were acquired in the period range of 0.003–1000 s. Induction coils (Metronix MFS05) and non-polarized Pb/PbCl telluric electrodes were employed to measure two components of magnetic and two components of electric field respectively. Dipole lengths varied between 50 and 100 m. At each site overnight recordings were performed with

two sample rates, 1000 Hz and 20 Hz. Only the 1000 Hz sampled data from 00:00 to 02:00 local time (GMT + 3) were used to estimate magnetotelluric transfer functions for the higher frequencies. Industrial noise is less during the night and the signal from equatorial thunderstorm activity is high, therefore providing better data quality All 20 Hz data files were merged together to form one day continuous recording. All data were processed with a robust remote reference code (Smirnov, 2003). Almost for all sites both the single station and remote reference magnetotelluric transfer functions were estimated. After the first set of recordings along the profile A, we decreased the site spacing from 2 km to 1 km when the results indicated that we are close to a geoelectrical discontinuity.

The level of industrial EM noise in the area was generally low. In the frequency range of 300 Hz–5 Hz, the single site (SS) estimates coincide very well with the remote reference (RR) estimates. Certain improvement was achieved in the period range of 0.1–20 s (dead band). Therefore we have used RR estimates to derive the final results.

The quality of the transfer functions was controlled by the 1-D inversion of the individual off-diagonal elements of the impedance tensor as well as of the determinant average. Thus the consistency between apparent resistivity and impedance phase estimates, which are related via dispersion relations (Fischer† and Schnegg†, 2007) were checked for all data. If no obvious problems were found, data were accepted for the further interpretation.

4. Strike and dimensionality analysis

In our analysis we rely upon the application of a routine 2-D inversion of MT data collected along profiles. Before inverting the data, it is necessary to get information about the dimensionality of the underlying structure in order to understand the deviation from the assumed 2D model. Moreover in order to interpret the magnetotelluric data with 2-D models, it is important to find a correct strike for every geoelectrical structure under examination. Standard bimodal 2-D inversion requires decomposition of impedance tensor into E and H polarizations. However, in practice, due to 3-D effects in the data, the decomposition is not perfect which may lead to data that are impossible to fit as well as may produce spurious models (Becken et al., 2008b).

Determination of the correct strike is still of importance even for the determinant inversion. A wrong strike causes the model (distances along the selected profile) to be expanded relative to the 'true' 2D model by a factor of Xs = 1 / cos(a), where a is the angle between true and selected strikes. This results in a wrong geometry of the model and also distorted resistivities.

To obtain quantitative estimate of the deviation from two-dimensionality as well as strike direction we applied Q-function analysis of Zhang et al. (1987) further explored by Smirnov and Pedersen (2008). The analysis involves least squares (LS) minimization of a quadratic objective function (Q), constructed within selected frequency range and selected sites:

$$Q = \sum\sum Q_{ij}$$
$$Q_{ij} = \left|Z_{xx} - \beta Z_{yx}\right|^2 + \left|Z_{yy} - \gamma Z_{xy}\right|^2 \quad (1)$$

where index *i* refers to the stations and index *j* to the periods over which the averaging is done, β and γ parameters are real galvanic distortion parameters, which in the case of a regional 2-D structure with strike direction along the x-axis have the following simple physical interpretation: β is the ratio between the electric field along strike to the horizontal electric field perpendicular to strike (B polarization) and γ is the ratio between the horizontal electric field perpendicular to strike to the electric field along strike (E polarization). Objective function (1) attains its minima in the regional strike direction. The quality of the 2-D assumption for the chosen strike is given by the normalized Q-function.

In our analysis we selected to minimize the Q function over one decade separately for each site, which is a reasonable assumption for a given site distances for each profile A, B and C (Fig. 2). Due to the 90° ambiguities a priori geological information concerning the geoelectric strike is required. Therefore, for profile A, a preferred geoelectric strike of N130°E is selected for the Atalanti fault. From the MT data, a constant geoelectric strike is defined for profile B, which equals to N120°E. On the other hand, the data analysis for the profile C shows N90°E geoelectric strike. The latter significantly deviates from the WNW–ESE strike found along the two other profiles possibly due to the existence of an ENE–WSW or NE–SW cross fault that affects the Atalanti fault in the NW part.

Additionally, we calculated the normalized $\sqrt{Q_{ij}}$ function for the selected strike with a 5% error for the impedance tensor elements (Fig. 3). For most periods/sites $\sqrt{Q_{ij}}$ is less than 2, meaning that data satisfy necessary 2-D conditions within 10% error. In conclusion, the dimensionality and strike analysis show a determinable geoelectric strike for all the profiles allowing further 2-D data interpretation.

However, one should keep in mind, as the strike analysis shows that there are some distortion effects in some specific frequencies and sites. Especially in profile C, where √Qij values are high for low frequencies, suggesting the existence of 3-D effects (Fig. 3).

5. 2-D inversion

In the present study, we based our interpretation on the determinant average data. The reason for this choice is that the strike direction is not fully stable from site to site and has a dependence on period in some sites. The determinant average is free from this uncertainty because it is invariant under rotation. Galvanic distortions just shift the amplitude of the determinant and leave the phase unchanged, i.e. the determinant phase is free of galvanic distortions.

However, the bimodal inversion was applied in order to see the differences with the determinant average data. The direction of the profiles was chosen to be N40°E for A and N30°E for B as defined from the strike analysis. A more complicated situation is at profile C, where the strike estimates seems to be determined by different structures, although the distortion analysis does not indicate strong 3D effects. The direction of the profile C was selected to coincide with measured sites, taking into account that it is close to the end of the fault and 3D effects prohibits a stable strike estimate as also denoted from the Q analysis. For this reason, the model for this profile should be interpreted with caution.

Two codes where applied to perform 2D inversion: (a) the Rodi and Mackie code (Rodi and Mackie, 2001) and (b) the Rebocc code by Siriponvaraporn and Egbert (2000) including the modifications made by Pedersen and Engels (2005) to allow for the inversion of the determinant of the impedance tensor. We used error floors of 5% for the impedance phase and 50% for the apparent resistivity in all variants of inversions. The higher error floor for the resistivity is chosen to allow the inversion procedure to compensate for the static shifts, since there was no other information in order to constrain the static shift and site spacing is relatively small. Bimodal inversion gave quite similar results for both codes and the final relative RMS (root mean square) reached was 3.1 for profile A. From the other hand the determinant data were fitted to RMS 1 for all profiles. Hence, based on the fact that we could not fit E and B polarizations, but determinant data, we based our interpretation on the results of the determinant inversion. Moreover, the general results of both inversions and the results of different codes do not contradict, but the results of the determinant inversion produced smoother model having smaller model norm. Also the problem of strike determination on C profile is not as critical for the determinant inversion as for the bimodal inversion.

As described above, profile A had a trend of N40°E onto which the 12 MT stations were projected. The inversion started with a homogeneous half space of 50 Ω m. The same procedure was followed for the

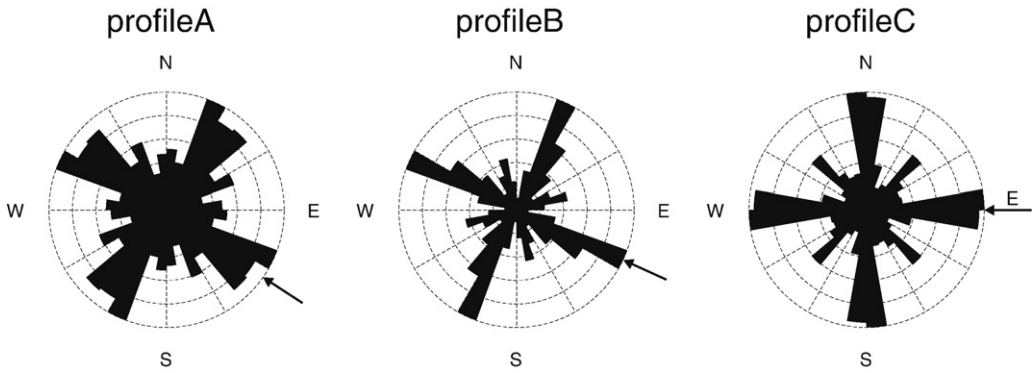

Fig. 2. Cumulative rose diagrams of strike directions from Q-function analysis from all sites in the period range of 0.01–100 s for all profiles. The resolution of rose diagrams is 10°. Q functions were minimized over one decade of periods for each site independently. An arrow for each profile indicates the selected strike direction. Dashed circles indicate the number of counts normalized.

other profiles B and C that cover the northern part of the study area. Profiles B and C comprises of nine sites and eight sites, respectively. The data misfits as well as observed and modeled transfer functions for all profiles are shown in Fig. 4. The resulting geoelectrical models are presented in Fig. 5.

6. Sensitivity tests and interpretational model

In order to better understand how observed anomalies are reliable and especially the geometrical characteristics, we performed a resolution test for the profiles A and B similar to what was adopted in Schwalenberg et al. (2002) and Smirnov and Pedersen (2008). The test included the setup of a priori models, where the resulted geoelectrical boundaries were altered. More precisely, in these models, the boundaries have been shifted laterally. Then we run the inversion to see whether such changes are in contradiction with measured data by comparing RMS misfit of initial iteration and the final iteration with final result of inversion without a priori models.

From this process, the resulted boundaries were juxtaposed with the initial ones. The RMS values of the inversion results with different a priori models were then compared. The main geoelectrical boundaries that are described below are well defined and especially the top of the conductive region, that is natural for EM methods. However, the following important features are somewhat less stable but are still required by the data: (a) the width of the transition zone between the conductor and the resistors in profile A, (b) the NNE part of the profile B is not well defined due to insufficient coverage of magnetotelluric stations, i.e. only one station, B9, exists.

Since at the profile C we have observed 3-D effects we have skipped the sensitivity tests for this profile. The results for this profile should therefore be interpreted with care.

Based on the sensitivity tests we derived the geometrical characteristics defined for each profile as follows:

Profile A

In this profile (Fig. 5a) the geoelectric stratigraphy can be derived from three distinct anomalies based on their resistivity, varying from less than 10 Ω m as highly conductive areas and more than few hundreds of Ω m as resistive areas. In particular, a low resistive body (B1) is overlaid by a high resistive body (B2) and the latter is followed upwards by a medium resistive body (B3). This geoelectrical stratigraphy is affected by two high-angle structures (F1, F2) dipping toward the NE that subdivide the region, from SW to NE, into three different domains, namely D1, D2 and D3. Due to these structures, the geoelectrical boundaries between B1 and B2, and B2 and B3 present an apparent subsidence toward the NE of a step-like geometry. This subsidence is more pronounced in the case of the boundary B1–B2 which presents a composite dip angle of about 30° toward the NE.

F1 structure is located beneath station 4 and F2 beneath stations 9–10 with dip angles at 60° and 76°, respectively, toward the NE. These

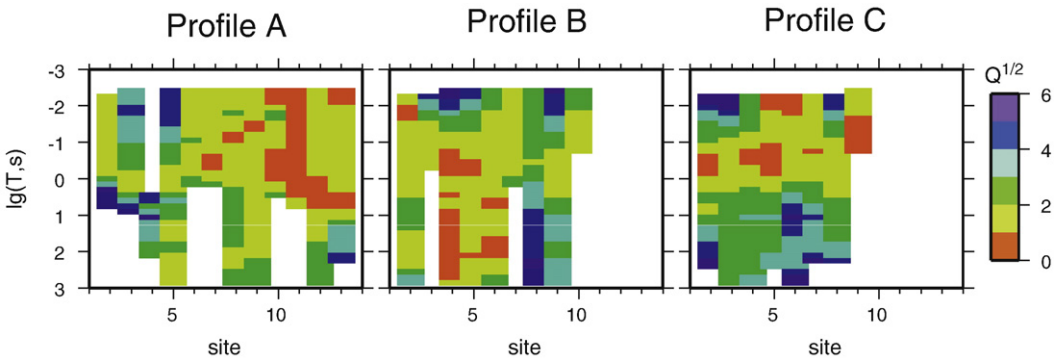

Fig. 3. √Q plots for the measured impedance tensor for N130°E, N120°E, and N0°E strike directions for (a) profile A, (b) profile B, and (c) profile B, respectively. The √Q-function represents a quantitative measure of the deviation of the impedance tensor from 2D conditions. Unity means that the impedance tensor elements satisfy 2D assumptions subject to the given error floor of 5%.

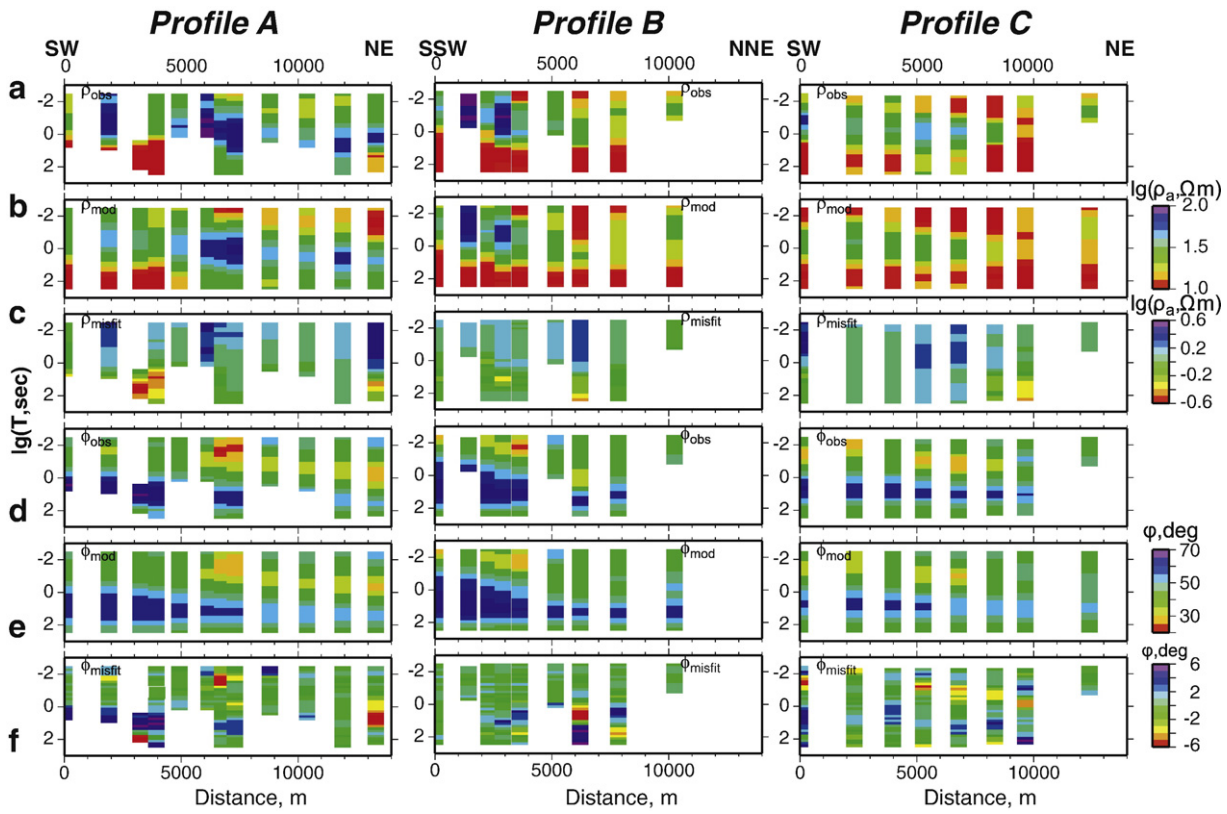

Fig. 4. Pseudo-sections of observed and model impedance determinant and their misfits (observed-model): (a) observed and (b) model apparent resistivities and (c) their corresponding misfits. (d) Observed and (e) model impedance phases and (f) their corresponding misfits.

structures are well traced to the depth of 4–5 km, whereas their inferred extension shows that they merge into a single structure at the depth of 10–12 km.

Profile B

The geoelectrical model NNE of station 8 is not robust due to the aforementioned deviations from two-dimensionality. However, a similar geoelectric stratigraphy containing B1, B2 and B3 bodies is recognized. Also, high-angle structures, similar to F1 and F2 of profile A, dipping at 60° and 80° toward the NNE, respectively are also detected. As profile A, the region is subdivided into three domains D1, D2 and D3 from SSW to NNE. In particular, F1 is located beneath stations 3–4 and F2 beneath station 6. Due to F1 structure, the B1–B2 geoelectrical boundary presents a peculiar, but similar subsidence toward the NNE, whereas the boundary B2–B3 is clearly traced only in domain D3. However, in domain D1 the boundary B1–B2 reveals similar dip angle with that of profile A.

In addition, F1 and F2 structures are well traced down to the depth of 5–6 km, where they merge into a single structure.

Profile C

In this profile, B1 and B2 bodies dominate the geoelectrical stratigraphy, whereas the overlying B3 body is traced at very surficial depths. The boundary B1–B2 is down to the depths of 2–3 km and only one fault structure can be defined in the geoelectrical section of profile C (Fig. 5). This implies that the F1 and F2 structures defined in profiles A and B should have been merged in a single structure at this part of the region. Consequently, this single structure F1-2 dips toward the NE at an angle of about 60° and it can be traced down to the depth of about 4 km.

As it is mentioned above, the geoelectrical strike for the stations on this profile is defined to be N90°E (Fig. 2). Because of this and the fact that the trend of the profile is N60°E, scaling effects in the inversion result exist. Indeed, based on the trigonometric equation

$$\tan(\alpha) = \tan(\delta) * \sin(\beta) \quad (2)$$

where α is the resulting dipping angle due to the scaling effect, δ is the original dipping angle (i.e. 76° as calculated for profile A), and β is the angle between the trend of the profile used and the defined geophysical strike (i.e., $90° - 60° = 30°$), we calculate an apparent dipping angle, $\alpha = 63.5°$. This angle is similar with that shown in Fig. 5c. However, this result should be interpreted cautiously.

An explanation for the geoelectrical strike deviation of this profile could be a NE–SW striking cross fault that disrupts the continuation between the Kalidromon and Atalanti fault segments of the KAM FZ (Fig. 1b).

7. Interpretation

Since our effort is to relate the geoelectrical models with the geology of the region, our interpretation is accomplished for each profile described above as follows:

Profile A

The F1 and F2 structures represent two distinct high-angle branches of the already known seismically active Atalanti fault joining each other at the depth of about 10–12 km. The B1 body that is characterized by low resistivity values should correspond to the carbonate sequence of the Parnassos zone or to the External Hellenides sensu lato that the carbonate rocks dominate their stratigraphy. However since the carbonate rocks do not reveal such low resistivity values, the conductance of B1 could be less probably due to the bauxite

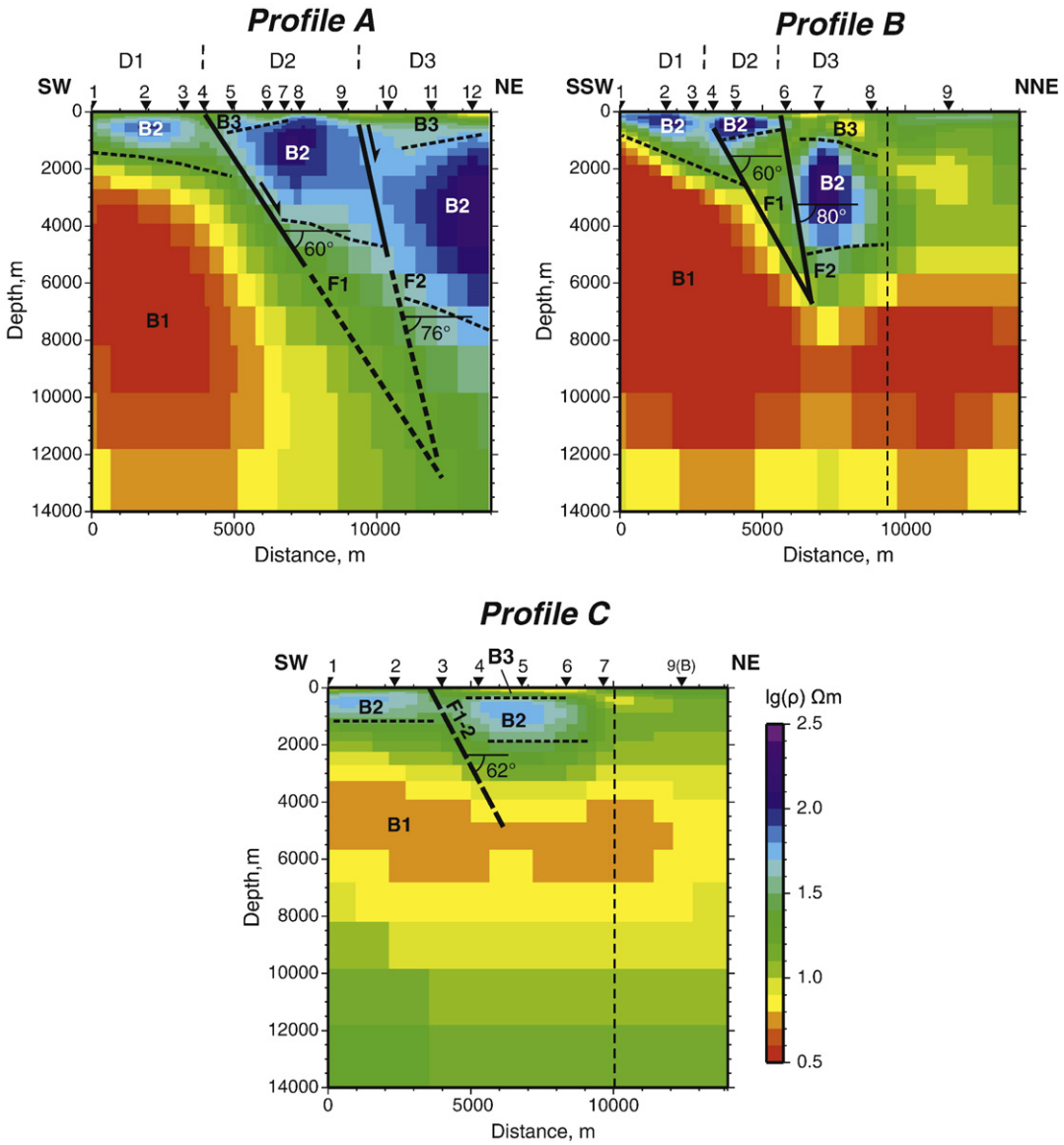

Fig. 5. Final resistivity models along the profiles A, B and C. The interpreted geoelectrical bodies are labeled with B1, B2, and B3 and the distinguished domains are labeled with D1, D2 and D3. The continuous lines correspond to defined faults and the dashed lines to their possible extension at depth. The dip angle of the faults is also shown. Interpreted geological boundaries are shown with dotted lines.

horizons of the Parnassos zone but most probably due to the fact that this body is a hydrothermal reservoir. The presence of the recent Plio-Quaternary volcanic activity and hydrothermal activity along the Sperchios–Arkitsa Fault Zone facilitates the latter mentioned interpretation (Andritsos et al., 2010; Apostolopoulos, 2005; Pe-Piper and Piper, 2002). The B2 body, which is characterized by high resistivity, corresponds to the ophiolite rocks and its underlying crystalline rocks of the Pelagonian and SubPelagonian zone. The B3 body represents the Neogene–Quaternary sedimentary cover resting onto the rocks of the Pelagonian and SubPelagonian zones, the thickness of which is varying between the different domains D2 and D3 where they expose.

An important issue of the interpretation of this profile is that the geoelectrical boundary B1–B2 is interpreted to be a low-angle overthrust between the underlying External Hellenides (Parnassos zone) and the overlying Internal Hellenides (Pelagonian and SubPelagonian zones) dipping at about 10°–20° toward the NE. This overthrust is detected at a depth of 2 km to the SW down to the depth of approximately 6 km to the NE as it is displaced by the Atalanti normal fault.

Profile B

In this profile, F1 and F2 structures also represent two high-angle fault branches of the Atalanti fault, dipping respectively at 60° and 80°, respectively to the NNE. These branches merge at the depth of approximately 5–6 km. Due to this, a displacement of about 4 km occurred along the Internal Hellenides overthrust.

Profile C

The interpretation of this profile is not as robust as the previous ones. However, the Atalanti fault could be traced as a single fault surface that dips at about 60° toward the NE. The boundary B1–B2 which corresponds to the Internal Hellenides overthrust is not accurately defined as it is in the previous profiles.

8. Discussion and conclusions

The application of the magnetotelluric method in a tectonically active region, where seismically active faults are exposed at the surface, revealed remarkable features related to the fault geometry. The method presents several advantages such as the direct and robust determination of the fault strike and the estimation of the fault dip angle.

As a result, the Atalanti fault that belongs to the Sperchios–Chalkis Fault System comprises two fault branches that both dip toward the NE with slightly different dip angles. The SW-most branch dips at about 60° and the NE-most branch dips at about 80°. These branches join each other below the depth of 5 km forming a single fault. A single fault is also formed along the strike of the fault and toward the NW direction as shown on the profile C. Although, the Atalanti fault at the surface displaces rocks belonging to the Internal Hellenides forming to the NE a sedimentary basin filled up by Neogene–Quaternary sediments, in depth, it laterally separates rocks (B1–D1) that belong to the External Hellenides (footwall) from rocks (B2–D2) that belong to the Internal Hellenides (hanging wall). More precisely, the Atalanti fault is a high-angle rupture zone that displaces in depth the Internal Hellenides overthrust that carries the rocks of the SubPelagonian and Pelagonian zones over the Parnassos zone. The subsidence of this overthrust due to the Atalanti fault is toward the NE and it is estimated as high as 4 km since its depth in the footwall is about 2 km, and in the hanging wall is about 6 km.

The interpretation presented herein suggests that the footwall of the Atalanti fault is the Parnassos zone of External Hellenides, a part of the External Hellenides that consists of a large hydrothermal reservoir.

Our suggestion that the Atalanti fault is a high-angle rupture zone is in accordance with the field observations of its exposure at the surface (Pavlides et al., 2004) and similar surface recordings made along the Kalidromon fault segment (Kranis, 2007).

The high-angle fault geometry imaged by the magnetotelluric method advocates that the Sperchios–Chalkis Fault System is a fault segment, which was originated as a high-angle fault zone and not as a low-angle extensional fault. Therefore, it is in agreement with the faulting processes proposed for the Corinth Gulf by Armijo et al. (1996) who also suggest that the Corinth Gulf Fault System was originated as a high-angle fault. It also contributes to the general view that the large NW–SE striking basins that were developed in the inner part of the Hellenic orogen since the Late Miocene should be attributed to the activation of similarly striking high-angle faults as already suggested for other NW–SE striking faults in that region (see for example Tranos, 2011).

The geophysical model proposed here is important, since it is the only model that provides information about the Atalanti fault at depth. Indeed, the available seismological data derived from different local experiments (Burton et al., 1991; Karamanos et al., 2010; Kemetzetzidou, 1996) were based on small earthquakes that occurred far away from the fault zone. It also defines the existence of the Parnassos zone in the footwall part of the Atalanti fault at a depth of 2 km and localizes the Alpine nappe tectonics in the wider region.

The existence of the two fault branches in the profiles A and B suggests that the Kalidromon–Atalanti–Martino Fault Zone is not a simple fault line as shown on maps (Fig. 1b) but consists of different fault segments and branches that in several places form wider damage zones such as the case of Atalanti fault.

References

Ambraseys, N.N., Jackson, J.A., 1990. Seismicity and associated strain of Central Greece between 1890 and 1988. Geophysical Journal International 101, 663–708.

Andritsos, N., Arvanitis, A., Papachristou, M., Fytikas, M., Dalambakis, P., 2010. Geothermal activities in Greece during 2005–2009. Proceedings World Geothermal Congress 2010, Bali, Indonesia, 25–29 April 2010.

Apostolopoulos, G., 2005. Geophysical studies relating to the tectonic structure, geothermal fields and geomorphological evolution of the Sperchios River Valley, Central Greece. Journal of the Balkan Geophysical Society 8 (3), 99–112.

Armijo, R., Mayer, B., King, G.C.P., Rigo, A., Papanastassiou, D., 1996. Quaternary evolution of the Corinth Rift and its implications for the Late Cenozoic evolution of the Aegean. Geophysical Journal International 126, 11–53.

Axen, G.J., Fletcher, J.M., Cowgill, E., Murphy, M., Kapp, P., MacMillan, I., Ramos-Velázquez, E., Aranda-Gómez, J., 1999. Range-front fault scarps of the Sierra El Mayor, Baja California: formed above an active low-angle normal fault? Geology 27, 247–250.

Becken, M., 2010. Review: magnetotelluric studies at the San Andreas Fault zone. IAGA WG 1.2 on Electromagnetic Induction in the Earth 20th Workshop. Giza, Egypt, September 18–24, 2010.

Becken, M., Ritter, O., Park, S.K., Bedrosian, P.A., Weckmann, U., Weber, M., 2008a. A deep crustal fluid channel into the San Andreas Fault system near Parkfield, California. Geophysical Journal International 173, 718–732.

Becken, M., Ritter, O., Burkhardt, H., 2008b. Mode separation of magnetotelluric responses in three-dimensional environments. Geophysical Journal International 172, 67–86.

Becken, M., Ritter, O., Bedrosian, P.A., Weckmann, U., 2011. Correlation between deep fluids, tremor and creep along the central San Andreas Fault. Nature 480, 7375 (87-U248).

Bedrosian, P., Unsworth, M., Egbert, G., 2002. Magnetotelluric imaging of the creeping segment of the San Andreas Fault near Hollister. Geophysical Research Letters 29 (11), 1506.

Burton, P., Makropoulos, K., McGonigle, R., Ritchie, M., Main, I., Kououskouna, V., Drakopoulos, J., 1991. Contemporary seismicity on the Nea Ankhialos Fault, Eastern Greece: fault parameters of major and minor earthquakes. Technical report WL/91/29, British Geological Survey, Seismology Series.

Collettini, C., 2011. The mechanical paradox of low-angle normal faults: current understanding and open questions. Tectonophysics 510, 253–268.

Fischer†, G., Schnegg†, P.-A., 2007. The magnetotelluric dispersion relations over 2-D structures. Geophysical Journal International 115 (3), 1119–1123.

Ganas, A., Roberts, G., Memou, T., 1998. Segment boundaries, the 1894 ruptures and strain patterns along the Atalanti Fault, Central Greece. Journal of Geodynamics 26, 461–486.

Goldsworthy, M., Jackson, J.A., 2001. Migration of activity within normal fault systems: examples from the Quaternary of mainland Greece. Journal of Structural Geology 23, 489–506.

Hatzfeld, D., 1999. The present-day tectonics of the Aegean as deduced from seismicity. Geological Society of London, Special Publications 156, 415–426.

Jackson, J.A., McKenzie, D.P., 1999. A hectare of fresh striations on the Arkitsa Fault, Central Greece. Journal of Structural Geology 21, 1–6.

Jones, A., Snyder, D., Hanmer, S., Asudeh, I., White, D., Eaton, D., Clarke, G., 2002. Magnetotelluric and teleseismic study across the Snowbird Tectonic Zone, Canadian Shield: a Neoarchean mantle suture? Geophysical Research Letters 29 (17), 1829.

Karamanos, Ch.K., Karakostas, V.G., Seeber, L., Papadimitriou, E.E., Kilias, A.A., 2010. Recent seismic activity in Central Greece revealing local seismotectonic properties. Bulletin of the Geological Society of Greece XLIII, 2075–2083.

Karastathis, V., Ganas, A., Makris, J., Papoulia, J., Dafnis, P., Gerolymatou, E., Drakatos, G., 2007. The application of shallow seismic techniques in the study of active faults: the Atalanti normal fault, Central Greece. Journal of Applied Geophysics 62, 215–233.

Kemetzetzidou, D., 1996. Etude sismotectonique du systeme Thessalie-iles Sporades (Grece-Central), Ph.D. Thesis, Observatorie de Grenoble, Laboratoire de Geophysiques Interne et Tectonophysique, Grenoble, (in French).

Kilias, A.A., Tranos, M.D., Papadimitriou, E.E., Karakostas, V.G., 2008. The recent crustal deformation of the Hellenic orogen in Central Greece; the Kremasta and Sperchios Fault Systems and their relationship with the adjacent large structural features. Zeitschrift der Deutschen Gesellschaft für Geowissenschaften 159/3, 533–547, http://dx.doi.org/10.1127/1860-1804/2008/0159-0533.

Kranis, H.D., 1999. Neotectonic Activity of Fault Zones in central-eastern Mainland Greece (Lokris). Ph.D. Thesis. GAIA 10, 2003.

Kranis, H.D., 2007. Neotectonic basin evolution in central-eastern mainland Greece: an overview. Bulletin of the Geological Society of Greece 40, 360–373.

Kranis, H.D., Papanikolaou, D., 2001. Evidence for detachment faulting on the NE Parnassos mountain front (Central Greece). Bulletin of the Geological Society of Greece XXXIV, 281–287.

Ledo, J., Jones, A., 2002. Electromagnetic images of a strike slip fault: the Tintina Fault — northern Canada. Geophysical Research Letters 29, 8.

Louvari, E., 2000. A detailed seismotectonic analysis of the Aegean and the surrounding area. Ph.D. thesis, Aristotle University of Thessaloniki, (in Greek).

Maercklin, N., Bedrosian, P.A., Haberland, C., Ritter, O., Ryberg, T., Weber, M., Weckmann, U., 2005. Characterizing a large shear-zone with seismic and magnetotelluric methods: the case of the Dead Sea Transform. Geophysical Research Letters 32, L15303, http://dx.doi.org/10.1029/2005GL022724.

Maratos, G., 1965. Geological map of Greece, Atalanti Sheet, scale 1:50,000, Institute of Geological and Exploration Research, Athens.

Mitsopoulos, K., 1895. The Lokris Mega-Earthquake in April 1894. National Printing House, Athens. (in Greek).

Mountrakis, D., 1986. The Pelagonian zone in Greece: a polyphase deformed fragment of the Cimmerian continent and its role in the geotectonic evolution of the Eastern Mediterranean. Journal of Geology 94, 335–347.

Mountrakis, D.M., 2010. Geology and Geotectonic Evolution of Greece. University Studio Press, Thessaloniki. (in Greek).

Mountrakis, D., Kilias, A., Pavlides, S., Zouros, N., Spyropoulos, N., Tranos, M., Soulakellis, N., 1993. Field study of the southern Thessaly highly active fault zone. Proceedings 2nd Geophys. Hellenic Geoph. Union, 2, pp. 603–614.

Mountrakis, D., Tranos, M., Papazachos, C., Thomaidou, E., Karagianni, E., Vamvakaris, D., 2006. New neotectonic and seismological data about the main active faults and stress regime of Northern Greece. In: Robertson, A.H.F., Mountrakis, D. (Eds.), Tectonic development of the eastern Mediterranean region: Journal of Geological Society, London, Special Publications, 260, pp. 649–670.

Pantosti, D., De Martini, P., Papanastassiou, D., Palyvos, N., Lemeille, F., Stavrakakis, G., 2001. A Reappraisal of the 1894 Atalanti earthquake surface ruptures, Central Greece. Bulletin of the Seismological Society of America 91, 760–780.

Pantosti, D., De Martini, P., Papanastassiou, D., Lemeille, F., Palyvos, N., Stavrakakis, G., 2004. Paleoseismological trenching across the Atalanti fault (Central Greece): evidence for the ancestors of the 1894 earthquake during the Middle and Roman times. Bulletin of the Seismological Society of America 94, 531–549.

Papanikolaou, D., Royden, 2007. Disruption of the Hellenic arc: Late Miocene extensional detachment faults and steep Pliocene–Quaternary normal faults — or what happened at Corinth? Tectonics 26, TC5003.

Papazachos, B., Papazachou, C., 2003. The Earthquakes of Greece. Ziti Publications.

Papazachos, B.C., Papadimitriou, E.E., Kiratzi, A.A., Papazachos, C.B., Louvari, E.K., 1998. Fault plane solutions in the Aegean Sea and the surrounding area and their tectonic implication. Bolletino di Geofisica Teorica ed Applicata 39, 199–218.

Papazachos, B., Mountrakis, D., Papazachos, C., Tranos, M., Karakaisis, G., Savvaidis, A., 2001. The faults which have caused the known major earthquakes in Greece and surrounding region between the 5th century BC and today. 2nd Hellenic Congress in Earthquake Engineering and Engineering Seismology, Thessaloniki 28–30 August 2001, A, pp. 17–26.

Pavlides, S., Valkaniotis, S., Ganas, A., Keramidas, D., Smporas, S., 2004. The Atalanti active fault — re-evaluation with new geological data. Proceedings of the 10th International Congress, Thessaloniki, April 2004. Bulletin of the Geological Society of Greece 36, 1560–1567.

Pedersen, L.B., Engels, M., 2005. Routine 2D inversion of magnetotelluric data using the determinant of the impedance tensor. Geophysics 70 (2), G33–G41.

Pe-Piper, G., Piper, D.J.W., 2002. The Igneous Rocks of Greece. The Anatomy of an Orogen. Beitrage zur "Regionalen Geologie der Erde (Series). Gebruder Borntraeger, Stuttgart. ISBN: 3 443 11030 4, http://dx.doi.org/10.1017/S0016756803218021. xvi + 573 pp.

Poulimenos, G., Doutsos, T., 1996. Barriers on seismogenic faults in central Greece. Journal of Geodynamics 22, 119–135.

Ritter, O., Ryberg, T., Weckmann, U., Hoffmann-Rothe, A., Abueladas, A., Garfunkel, Z., DESERT Research Group, 2003. Geophysical images of the Dead Sea Transform in Jordan reveal an impermeable barrier for fluid flow. Geophysical Research Letters 30 (14), 1741.

Ritter, O., Hoffmann-Rothe, A., Bedrosian, P.A., Weckmann, U., Haak, V., 2005. Electrical conductivity images of active and fossil fault zones. High Strain Zones: Structure and Physical Properties. The Geological Society, pp. 165–186.

Roberts, G.P., 1996. Variation in fault–slip directions along active and segmented normal fault systems. Journal of Structural Geology 6, 835–845.

Roberts, S., Jackson, J., 1991. Active normal faulting in Central Greece: an overview. In: Roberts, Yielding, Freeman (Eds.), The Geometry of Normal Faults: Geol. Soc. Spec. Publ. London, 56, pp. 125–142.

Rodi, W., Mackie, R.L., 2001. Nonlinear conjugate gradients algorithm for 2-D magnetotelluric inversion. Geophysics 66, 174–187.

Rondogianni-Tsiambaou, Th., 1984. Etude neotectonique des ravages occidentaux du canal d' Atalanti (Grece Central). Ph. D. Thesis, University de Paris, (in French).

Sakellariou, D., Rousakis, G., Kaberi, H., Kapsimalis, V., Georgiou, P., Kanelopoulos, Th., Lykousis, V., 2007. Tecto-sedimentary structure and late quaternary evolution of the north EVIA Gulf Basin, central Greece: preliminary results. Bull. of the Geological Society of Greece, XXXX, 2007, 11th International Congress, Athens.

Schwalenberg, K., Rath, V., Haak, V., 2002. Sensitivity studies applied to a two-dimensional resistivity model from the Central Andes. Geophysical Journal International 150, 673–686.

Siriponvaraporn, W., Egbert, G.D., 2000. An efficient data-subsurface inversion method for 2-D magnetotelluric data. Geophysics 65, 791–803.

Skouphos, T.G., 1894. Die zwei grossen Erdbeben in Lokris am 8/20 und 15/27 April 1894. Zeitschrift der Gesellschaft für Erdkunde zu Berlin 24, 409–474.

Smirnov, M., 2003. Magnetotelluric data processing with a robust statistical procedure having a high breakdown point. Geophysical Journal International 152, 1–7.

Smirnov, M.Yu., Pedersen, L.B., 2008. Magnetotelluric measurements across Sorgenfrei–Tornquist-zone in southern Sweden and Denmark. Geophysical Journal International 1762, 443–456.

Sorel, D., 2000. A Pleistocene and still-active detachment fault and the origin of the Corinth–Patras rift, Greece. Geology 28, 83–86.

Tranos, M.D., 2011. Strymon and Strymonikos Gulf basins (Northern Greece): implications on their formation and evolution from faulting. Journal of Geodynamics 51, 285–305, http://dx.doi.org/10.1016/j.jog.2010.10.002.

Unsworth, M., Bedrosian, P., 2004. Electrical resistivity at the SAFOD site from magnetotelluric exploration. Geophysical Research Letters 31.

Unsworth, M., Malin, P., Egbert, G., Booker, J., 1997. Internal structure of the San Andreas Fault at Parkfield, California. Geology 25 (4), 359–362.

Weber, M., et al., 2009. Anatomy of the Dead Sea Transform from lithospheric to microscopic scale. Reviews of Geophysics 47, RG2002, http://dx.doi.org/10.1029/2008RG000264.

Zhang, P., Roberts, R.G., Pedersen, L.B., 1987. Magnetotelluric strike rules. Geophysics 52, 267–278.